Research Article | Vol. 26, No. 23 | 12 Nov 2018 | OPTICS EXPRESS 31031
Optics EXPRESS

Spectrally interleaved topologies using geometric phase metasurfaces

MICHAEL YANNAI,[1] ELHANAN MAGUID,[1] ARKADY FAERMAN,[1] QITONG LI,[2] JUNG-HWAN SONG,[2] VLADIMIR KLEINER,[1] MARK L. BRONGERSMA,[2] AND EREZ HASMAN[1,*]

[1]*Micro and Nanooptics Laboratory, Faculty of Mechanical Engineering, and Russell Berrie Nanotechnology Institute, Technion – Israel Institute of Technology, Haifa 3200003, Israel*
[2]*Geballe Laboratory for Advanced Materials, Stanford University, 476 Lomita Mall, Stanford, CA 94305, USA*
**mehasman@technion.ac.il*

Abstract: Metasurfaces facilitate the interleaving of multiple topologies in an ultra-thin photonic system. Here, we report on the spectral interleaving of topological states of light using a geometric phase metasurface. We realize that a dielectric spectrally interleaved metasurface generates multiple interleaved vortex beams at different wavelengths. By harnessing the space-variant polarization manipulations that are enabled by the geometric phase mechanism, a vectorial vortex array is implemented. The presented interleaved topologies concept can greatly enhance the functionality of advanced microscopy and communication systems.

1. Introduction

Metasurfaces are two dimensional photonic devices consisting of arrays of subwavelength-scale nano-antennas, capable of manipulating light by controlling the local properties of an incident electromagnetic wave, including its amplitude, phase, polarization and momenta [1–8]. The latter encompasses the intrinsic angular momentum of the output beam [9,10], which facilitates the formation of various topological states of light – optical vortex beams and vectorial vortices. Advantageously, metasurfaces give us the ability to combine multiple functionalities in a single ultra-thin device. This capability was demonstrated in broadband systems, where all antennas share the same spectral response, using various techniques including segmentation and interleaving of sparse arrays, with applications in communications, sensing and beam characterization [11–17]. By controlling the spectral response of the nano-antennas [18–20], additional degrees of freedom are added to the system, enabling the spatial multiplexing of wavelength sensitive nano-antennas – spectrally-interleaved and multi-functional metasurfaces [21–27].

Here, we report on the spectral interleaving of topological states of light using a geometric phase metasurface (GPM). Generation of multiple interleaved vortex beams at different wavelengths from a single efficient spectrally-interleaved nano-device is demonstrated. The vectorial nature of the geometric phase is utilized to generate a vectorial vortex array, consisting of two distinct topologies at different wavelengths.

GPMs are composed of anisotropic antennas which generate a local spin-dependent phase delay defined by $\phi_g(x,y) = -2\sigma\theta(x,y)$ [1,2,6,28,29]. Here, $\theta(x,y)$ is the in-plane orientation angle of the antennas, and σ denotes the spin angular momentum of light $(\hbar\sigma)$, i.e., right $(\sigma = 1)$ or left $(\sigma = -1)$ circular polarization [9,10]. Due to the interaction with the antennas of varying orientations, the light's polarization state attained at different points across the GPM traverses various paths upon the Poincaré sphere. This results in a Pancharatnam–Berry phase pick-up between any pair of antennas, which is equal to half the

#346194 https://doi.org/10.1364/OE.26.031031
Journal © 2018 Received 18 Sep 2018; revised 1 Nov 2018; accepted 1 Nov 2018; published 9 Nov 2018

Optics EXPRESS

area of the corresponding geodesic triangle bounded by these paths on the Poincaré sphere [1,2].

2. Experimental results and discussion

Spectrally-interleaved GPMs are realized using dielectric subwavelength-scale antennas, which offer low loss and arbitrary control over the phase pick-up [6,14,30,31]. These are generated by the incorporation of two or more antenna types into an optimally spaced interleaved array. Here, the interleaved array is patterned into a crystalline silicon layer bonded to a borosilicate glass substrate. It is composed of two sub-arrays – a Kagome and a hexagonal lattice, each with its own resonant nano-antenna geometry (Fig. 1(a)). By using the Kagome and hexagonal lattices, and with proper selection of the lattice periods, no antennas need to be moved or removed in the interleaving process. This leads to minimal loss in efficiency when interleaving the two lattices, compared to the single-function efficiency.

To evaluate the performance of the spectrally-interleaved GPM, we measured the diffraction efficiency spectra for a GPM consisting of two spatially-separated linear phase profiles (Fig. 1(b)). Green and red spectra correspond to the antennas belonging to the Kagome and hexagonal lattices, respectively. Here, the diffraction efficiency is defined as the fraction of the intensity in the desired diffraction order, out of the total intensity at the GPM's output. The results are in good agreement with the simulated diffraction efficiency spectra, attained using finite-difference time-domain (FDTD) simulations.

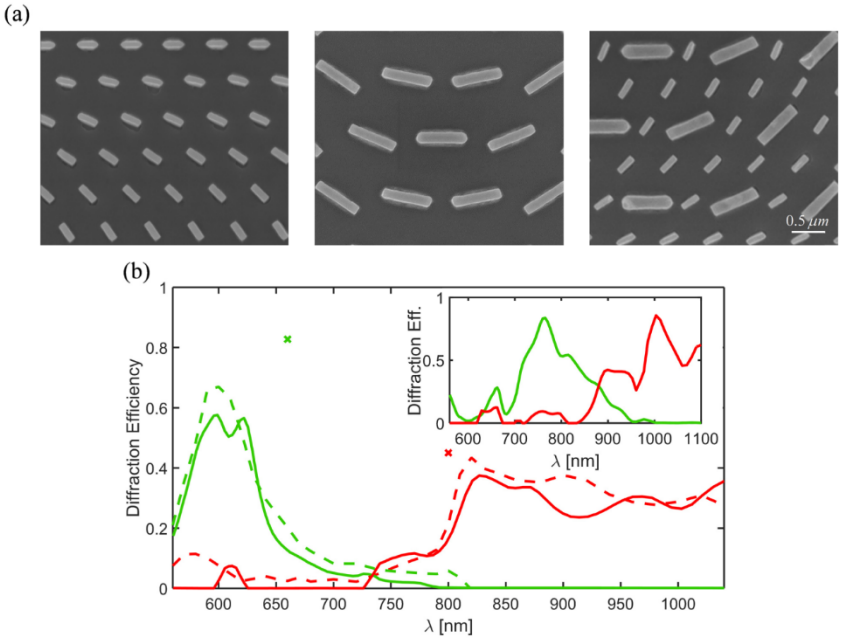

Fig. 1. Spectrally-interleaved GPM. (a) SEM images of the fabricated single- (left, center) and dual-function (right) spectrally-interleaved GPM. The first (second) nano-antenna with in-plane dimensions of 155 x 40 nm (420 x 110 nm) has a peak efficiency at a wavelength of 600 nm (820 nm) and is arranged into a Kagome (hexagonal) lattice with a lattice constant of 400 nm (800 nm). The nano-antennas' height is 400 nm throughout. (b) Diffraction efficiency spectra for a dual-function spectrally-interleaved GPM obtained via FDTD simulations (lines) and measurements (dashed lines). Crosses represent measured peak efficiencies for the single-function GPMs, attained at a wavelength of 660 nm (green) and 800 nm (red). The simulated antenna parameters were taken from the SEM images in (a). Inset shows diffraction efficiency spectra for the designed (optimal) antennas, obtained via FDTD simulations. The designed in-plane dimensions are 210 x 70 nm and 470 x 150 nm, with periods of 385 nm and 770 nm, respectively, and an antenna height of 400 nm.

Optics EXPRESS

By comparing the diffraction efficiency of one function at its peak efficiency wavelength to the diffraction efficiency of the other at that wavelength, a negligible cross-talk between the two spectral nano-antenna sub-arrays is clearly observed, both in simulation and measurement; The measured peak efficiency wavelengths are 600 nm and 820 nm. The loss in efficiency and spectral shifts are attributed to fabrication errors in the nano-antennas' dimensions. Simulated diffraction efficiency spectra in Fig. 1(b) take some of the dimensional errors into account, by using the actual dimensions of the fabricated nano-antennas. The simulated diffraction efficiency spectra for a spectrally-interleaved GPM consisting of the optimal antennas are presented in Fig. 1(b), inset. Simulated average spectral transmittance of 80% is obtained for the single- and dual-function spectrally-interleaved GPMs. Moreover, incorporating the two antenna sub-arrays has little effect on the individual functions' peak efficiency, as seen from the crosses in Fig. 1(b), which represent measured peak efficiencies for the single-function GPM's. Therefore, utilizing our spectral interleaving approach facilitates the generation of an efficient multi-functional metasurface.

Spectrally-interleaved GPMs can be utilized for the spatial multiplexing of various topologies, such as orbital angular momentum (OAM) carrying beams (scalar vortices) [12,14,32]. This class of beams, possessing a phase singularity, is of special interest for optical communication systems, optical tweezers, tractor beams, and laser beam shaping [33–38]. A scalar vortex is defined by the phase function $\exp(il\varphi)$, where l is the beam's topological charge $(l=\pm1,\pm2,...)$ and φ is the azimuthal angle. Due to the geometric phase's spin-dependent nature, an inherent coupling between the incident spin state and the topological charge occurs, leading to a spin-dependent topological charge of the output wavefront (σl).

We propose a simple and efficient method for the generation of multiple interleaved vortex beams. For this purpose, we designed a spectrally-interleaved GPM using the harmonic response (HR) approach, which is based on Dammann gratings [12,14,39]. These phase gratings are optimized to produce a finite number of diffraction orders with identical intensities $\left|A_j\right|^2$. To achieve this, the desired phase function ϕ_{HR} is expressed in terms of a set of harmonics $\exp\left(i\phi_{HR}(x,y)\right)\cong\sum_j A_j\exp\left(ik_j x\right)$, where k_j is the momentum redirection of the j[th] order. We use a particular analytic solution proposed by Gori [40], to achieve maximal diffraction efficiency for $-1\le j\le1$. This solution is expanded into two dimensions, and an orbital phase term is added, thus leading to a 3-by-3 array of harmonic orders $\phi_{HR}(x,y)\cong\tan^{-1}\left(\mu\cos(kx)\right)+\tan^{-1}\left(\mu\cos(ky)\right)+l\varphi$. Here, $\mu=2.65718$ and k is the momentum redirection. Each of the two sub-arrays was assigned with the above HR phase function, where for the short wavelength the topological charge l was set to zero, and for the long wavelength l was set to one (Fig. 2(a)). We illuminated the fabricated multiplexed-topologies GPM with circularly polarized light at a wavelength of 600 nm and 820 nm, and the two wavelength dependent phase functions were subsequently observed in momentum-space (Fig. 2(b)).

GPMs enable space-variant polarization manipulations, supporting the generation of vectorial vortex beams, which are formed by the coherent superposition of scalar vortices of opposite helicities and opposite spins [14,37,38,41,42]. This superposition is attained by illuminating a scalar vortex GPM with linearly polarized light, which can be described as a superposition of right and left circular polarizations. The resultant beam is characterized by axially-symmetric polarization states, and is defined by $\exp(-il\varphi)\left|\sigma_+\right\rangle+\exp(il\varphi+\Delta\phi)\left|\sigma_-\right\rangle$; here $\Delta\phi=\{0,\pi\}$ corresponds to radial and azimuthal polarizations, respectively, and $\left|\sigma_\pm\right\rangle$ denotes right and left circular polarization states.

Optics EXPRESS

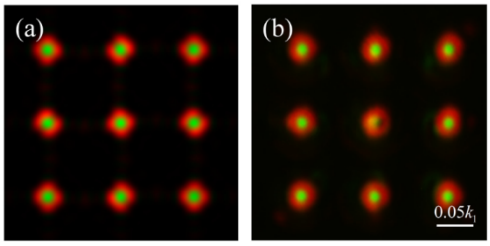

Fig. 2. Multiplexed-topologies GPM under circularly polarized illumination. (a) Simulated momentum-space intensity pattern of the multiplexed-topologies GPM obtained using a numerical model and the HR phase function. (b) Measured momentum-space intensity pattern of the fabricated GPM. The GPM was illuminated at a wavelength of 600 nm (green) and 820 nm (red). Images are false-colored. Here, $k_1 = 2\pi/\lambda_1$, where $\lambda_1 = 600$ nm.

Spectrally-interleaved GPMs facilitate the generation of multiple wavelength dependent vectorial vortices. In the proposed multiplexed-topologies GPM, using the HR approach leads to a phase difference between the right and left circular polarization phase functions, depending on the diffraction order's position in the 3-by-3 array. Therefore, each $l = 1$ diffraction order possesses either a radial or an azimuthal polarization state, corresponding to 0 or π phase difference, respectively. Furthermore, each $l = 0$ diffraction order is either vertically or horizontally polarized.

Due to the axial symmetry of the vectorial vortex states, projecting a vectorial vortex on a linear state using a polarizer reveals a petal-shaped diffraction pattern, which rotates when the output (or input) linear polarization angle is altered. Thus, by illuminating the multiplexed-topologies GPM with linearly polarized light, and performing a post-projection using a second polarizer at the output, linearly polarized $l = 0$ diffraction orders are observed in momentum-space, along with the rotating petal-shaped diffraction orders of the $l = 1$ function (Fig. 3).

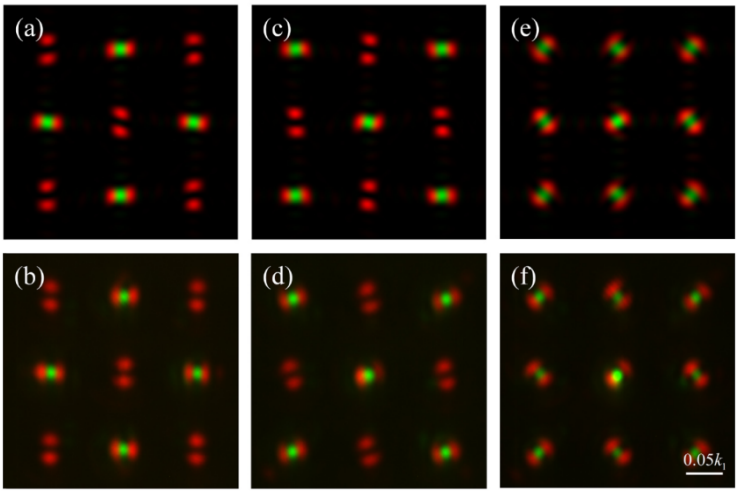

Fig. 3. Multiplexed-topologies GPM generating a vectorial vortex array. Simulated (a,c,e) and measured (b,d,f) momentum-space intensity patterns of the multiplexed-topologies GPM under linearly polarized illumination and horizontal (a,b), vertical (c,d) and diagonal (e,f) analyzer orientation. The GPM was illuminated at a wavelength of 600 nm (green) and 820 nm (red). Images are false-colored.

This behavior is further illustrated in Figs. 4(a) and 4(b) which depict the space-variant orientation angle ψ of the polarization ellipse, calculated from Stokes parameters

Optics EXPRESS

measurements of the $l=0$ and $l=1$ diffraction orders, respectively. Here, the orientation angle is defined by $\psi = \frac{1}{2}\tan^{-1}\left(S_2/S_1\right)$, where $S_1 = I_0 - I_{90}$ and $S_2 = 2I_{45} - I_0 - I_{90}$ are the first and second Stokes polarization parameters, and I_φ are the momentum-space intensity distributions attained after passing the output beams through a polarizer at an angle φ (see Figs. 3(b), 3(d) and 3(f)).

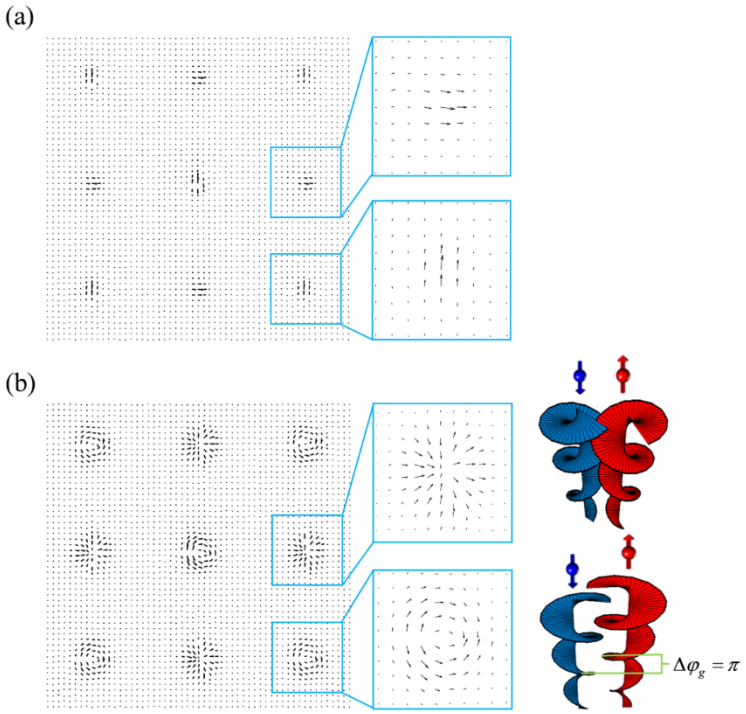

Fig. 4. Orientation angle analysis of the vectorial vortex array. (a,b) Vector field illustration of the space-variant orientation angle ψ for the $l=0$ (a) and $l=1$ (b) functions, obtained from momentum-space measurements of the Stokes parameters. Blue-framed insets show magnifications of two selected modes. Right insets illustrate the zero (top) or π (bottom) phase difference between opposite spins, generated by the HR phase and leading to radially and azimuthally polarized modes, respectively.

3. Concluding remarks

The spatial multiplexing of different topologies via spectrally-interleaved GPMs can find applications in microscopic imaging techniques, such as stimulated-emission-depletion (STED) fluorescence microscopy [43,44], where similarly structured light is utilized to enhance the spatial resolution beyond the diffraction limit. Our multiplexed-topologies GPM can be used to increase the system's throughput, by conducting parallel scanning of multiple sites within the sample at different polarizations. The multiplexing of wavelength, orbital angular momentum and polarization can greatly elevate the information capacity of fiber and free-space communication systems [33,45,46].

4. Methods

4.1 Sample fabrication

400-nm-thick single crystalline silicon slab on borosilicate glass substrate has been prepared by thinning a 20-μm-thick single crystalline silicon bonded to a borosilicate glass wafer (Plan

Optics EXPRESS

Optik AG) in two different dry etching processes. Initially, it is coarsely etched down to ~2 μm by deep reactive ion etching. It is then precisely thinned down to 400 nm by precise reactive ion etching. We use a spin-coated 70-nm-thick hydrogen silsesquioxane (HSQ) layer as a negative tone electron beam resist and the patterns are drawn by the electron beam lithography process (JEOL 6300 100 kV system). In order to reduce the charging effects, a conductive polymer layer (E-Spacer 300Z) is also used. Typical electron beam dose is set to be ~2000 μCcm^{-2} and the development is performed in 25% tetramethylammonium hydroxide (TMAH) for 2 minutes to form HSQ hard mask patterns. Precise reactive ion etching transfers the HSQ hard mask patterns into the silicon slab and the remaining HSQ hard mask pattern is ultimately removed using diluted 2% hydrogen fluoride (HF) solution for 1 minute to finish the fabrication.

4.2 Measurement procedure

A similar setup was used for all experiments mentioned. The input beam, generated by a supercontinuum laser source (Fianium Supercontinuum SC450) was temporally modulated by an acousto-optic modulator (Fianium AOTF V1) facilitating the use of multi-wavelength laser light. The beam was then spatially filtered and collimated. A linear polarizer (Pol.) followed by a quarter wave plate (QWP) serve as a circular polarizer. Two objectives in a 4f configuration are used to focus light onto the sample (GPM) and collect the scattered light, respectively. For the experiments depicted in Figs. 2–4, a polarizer-analyzer in a cross-polarized configuration is introduced, to eliminate the non-interacting diffraction order. Finally, the images are captured using a CMOS camera. Measurements of the diffraction efficiency and transmittance spectra are carried by removing the polarizer-analyzer.

Funding

United States–Israel Binational Science Foundation (BSF); Israel Science Foundation (ISF); US Air Force Office of Scientific Research (FA9550-18-1-0208) Photonic Metamaterials program; National Science Foundation (NSF) (ECCS-1542152); Jung-Hwan Song is supported by Basic Science Research Program through the National Research Foundation of Korea (NRF) funded by the Ministry of Education (NRF-2016R1A6A3A03012480).

Acknowledgments

The metasurfaces' fabrication was performed at the Stanford Nano Shared Facilities (SNSF) and at the Micro-Nano Fabrication & Printing Unit (MNF&PU), Technion.

References

1. Z. Bomzon, V. Kleiner, and E. Hasman, "Pancharatnam-Berry phase in space-variant polarization-state manipulations with subwavelength gratings," Opt. Lett. **26**(18), 1424–1426 (2001).
2. Z. Bomzon, G. Biener, V. Kleiner, and E. Hasman, "Space-variant Pancharatnam-Berry phase optical elements with computer-generated subwavelength gratings," Opt. Lett. **27**(13), 1141–1143 (2002).
3. A. Papakostas, A. Potts, D. M. Bagnall, S. L. Prosvirnin, H. J. Coles, and N. I. Zheludev, "Optical manifestations of planar chirality," Phys. Rev. Lett. **90**(10), 107404 (2003).
4. N. Yu, P. Genevet, M. A. Kats, F. Aieta, J.-P. Tetienne, F. Capasso, and Z. Gaburro, "Light propagation with phase discontinuities: generalized laws of reflection and refraction," Science **334**(6054), 333–337 (2011).
5. A. V. Kildishev, A. Boltasseva, and V. M. Shalaev, "Planar photonics with metasurfaces," Science **339**(6125), 1232009 (2013).
6. D. Lin, P. Fan, E. Hasman, and M. L. Brongersma, "Dielectric gradient metasurface optical elements," Science **345**(6194), 298–302 (2014).
7. A. E. Minovich, A. E. Miroshnichenko, A. Y. Bykov, T. V. Murzina, D. N. Neshev, and Y. S. Kivshar, "Functional and nonlinear optical metasurfaces," Laser Photonics Rev. **9**(2), 195–213 (2015).
8. Q. Wang, E. T. F. Rogers, B. Gholipour, C. M. Wang, G. Yuan, J. Teng, and N. I. Zheludev, "Optically reconfigurable metasurfaces and photonic devices based on phase change materials," Nat. Photonics **10**(1), 60–65 (2016).
9. K. Y. Bliokh, F. J. Rodríguez-Fortuño, F. Nori, and A. V. Zayats, "Spin-orbit interactions of light," Nat. Photonics **9**(12), 796–808 (2015).

Optics EXPRESS

10. K. Y. Bliokh, D. Smirnova, and F. Nori, "Quantum spin Hall effect of light," Science **348**(6242), 1448–1451 (2015).
11. D. Veksler, E. Maguid, N. Shitrit, D. Ozeri, V. Kleiner, and E. Hasman, "Multiple wavefront shaping by metasurface based on mixed random antenna groups," ACS Photonics **2**(5), 661–667 (2015).
12. E. Maguid, I. Yulevich, D. Veksler, V. Kleiner, M. L. Brongersma, and E. Hasman, "Photonic spin-controlled multifunctional shared-aperture antenna array," Science **352**(6290), 1202–1206 (2016).
13. M. Q. Mehmood, S. Mei, S. Hussain, K. Huang, S. Y. Siew, L. Zhang, T. Zhang, X. Ling, H. Liu, J. Teng, A. Danner, S. Zhang, and C. W. Qiu, "Visible-frequency metasurface for structuring and spatially multiplexing optical vortices," Adv. Mater. **28**(13), 2533–2539 (2016).
14. E. Maguid, I. Yulevich, M. Yannai, V. Kleiner, M. L Brongersma, and E. Hasman, "Multifunctional interleaved geometric-phase dielectric metasurfaces," Light Sci. Appl. **6**(8), e17027 (2017).
15. F. Ding, A. Pors, Y. Chen, V. A. Zenin, and S. I. Bozhevolnyi, "Beam-size-invariant spectropolarimeters using gap-plasmon metasurfaces," ACS Photonics **4**(4), 943–949 (2017).
16. M. Khorasaninejad and F. Capasso, "Metalenses: versatile multifunctional photonic components," Science 358(6367), 8100 (2017).
17. Y. Chen, F. Ding, V. Coello, and S. I. Bozhevolnyi, "On-chip spectropolarimetry by fingerprinting with random surface arrays of nanoparticles," ACS Photonics **5**(5), 1703–1710 (2018).
18. I. Staude, A. E. Miroshnichenko, M. Decker, N. T. Fofang, S. Liu, E. Gonzales, J. Dominguez, T. S. Luk, D. N. Neshev, I. Brener, and Y. Kivshar, "Tailoring directional scattering through magnetic and electric resonances in subwavelength silicon nanodisks," ACS Nano **7**(9), 7824–7832 (2013).
19. H.-S. Ee, J.-H. Kang, M. L. Brongersma, and M.-K. Seo, "Shape-dependent light scattering properties of subwavelength silicon nanoblocks," Nano Lett. **15**(3), 1759–1765 (2015).
20. A. I. Kuznetsov, A. E. Miroshnichenko, M. L. Brongersma, Y. S. Kivshar, and B. Luk'yanchuk, "Optically resonant dielectric nanostructures," Science **354**(6314), aag2472 (2016).
21. A. Arbabi, Y. Horie, A. J. Ball, M. Bagheri, and A. Faraon, "Subwavelength-thick lenses with high numerical apertures and large efficiency based on high-contrast transmitarrays," Nat. Commun. **6**(1), 7069 (2015).
22. B. Wang, F. Dong, Q.-T. Li, D. Yang, C. Sun, J. Chen, Z. Song, L. Xu, W. Chu, Y.-F. Xiao, Q. Gong, and Y. Li, "Visible-frequency dielectric metasurfaces for multiwavelength achromatic and highly dispersive holograms," Nano Lett. **16**(8), 5235–5240 (2016).
23. C. Huang, W. Pan, X. Ma, and X. Luo, "Multi-spectral metasurface for different functional control of reflection waves," Sci. Rep. **6**(1), 23291 (2016).
24. E. Arbabi, A. Arbabi, S. M. Kamali, Y. Horie, and A. Faraon, "Multiwavelength polarization-insensitive lenses based on dielectric metasurfaces with meta-molecules," Optica **3**(6), 628–633 (2016).
25. O. Avayu, E. Almeida, Y. Prior, and T. Ellenbogen, "Composite functional metasurfaces for multispectral achromatic optics," Nat. Commun. **8**, 14992 (2017).
26. B. Wang, F. Dong, D. Yang, Z. Song, L. Xu, W. Chu, Q. Gong, and Y. Li, "Polarization-controlled color-tunable holograms with dielectric metasurfaces," Optica **4**(11), 1368–1371 (2017).
27. Z. Shi, M. Khorasaninejad, Y. W. Huang, C. Roques-Carmes, A. Y. Zhu, W. T. Chen, V. Sanjeev, Z. W. Ding, M. Tamagnone, K. Chaudhary, R. C. Devlin, C. W. Qiu, and F. Capasso, "Single-layer metasurface with controllable multiwavelength functions," Nano Lett. **18**(4), 2420–2427 (2018).
28. S. Pancharatnam, "Generalized theory of interference and its applications," Proc. Indian Acad. Sci. A **44**(6), 398–417 (1956).
29. M. V. Berry, "The adiabatic phase and Pancharatnam's phase for polarized light," J. Mod. Opt. **34**(11), 1401–1407 (1987).
30. A. Arbabi, Y. Horie, M. Bagheri, and A. Faraon, "Dielectric metasurfaces for complete control of phase and polarization with subwavelength spatial resolution and high transmission," Nat. Nanotechnol. **10**(11), 937–943 (2015).
31. K. E. Chong, I. Staude, A. James, J. Dominguez, S. Liu, S. Campione, G. S. Subramania, T. S. Luk, M. Decker, D. N. Neshev, I. Brener, and Y. S. Kivshar, "Polarization-independent silicon metadevices for efficient optical wavefront control," Nano Lett. **15**(8), 5369–5374 (2015).
32. G. Biener, A. Niv, V. Kleiner, and E. Hasman, "Formation of helical beams by use of Pancharatnam-Berry phase optical elements," Opt. Lett. **27**(21), 1875–1877 (2002).
33. J. Wang, J. Y. Yang, I. M. Fazal, N. Ahmed, Y. Yan, H. Huang, Y. Ren, Y. Yue, S. Dolinar, M. Tur, and A. E. Willner, "Terabit free-space data transmission employing orbital angular momentum multiplexing," Nat. Photonics **6**(7), 488–496 (2012).
34. V. Shvedov, A. R. Davoyan, C. Hnatovsky, N. Engheta, and W. Krolikowski, "A long-range polarization-controlled optical tractor beam," Nat. Photonics **8**(11), 846–850 (2014).
35. J. Sun, X. Wang, T. Xu, Z. A. Kudyshev, A. N. Cartwright, and N. M. Litchinitser, "Spinning light on the nanoscale," Nano Lett. **14**(5), 2726–2729 (2014).
36. P. Miao, Z. Zhang, J. Sun, W. Walasik, S. Longhi, N. M. Litchinitser, and L. Feng, "Orbital angular momentum microlaser," Science **353**(6298), 464–467 (2016).
37. R. Chriki, E. Maguid, C. Tradonsky, V. Kleiner, A. A. Friesem, N. Davidson, and E. Hasman, "Spin-controlled twisted laser beams: intra-cavity multi-tasking geometric phase metasurfaces," Opt. Express **26**(2), 905–916 (2018).

Optics EXPRESS

38. E. Maguid, R. Chriki, M. Yannai, V. Kleiner, E. Hasman, A. A. Friesem, and N. Davidson, "Topologically controlled intracavity laser modes based on Pancharatnam-Berry phase," ACS Photonics **5**(5), 1817–1821 (2018).
39. H. Dammann and K. Görtler, "High-efficiency in-line multiple imaging by means of multiple phase holograms," Opt. Commun. **3**(5), 312–315 (1971).
40. F. Gori, M. Santarsiero, S. Vicalvi, R. Borghi, G. Cincotti, E. Di Fabrizio, and M. Gentili, "Analytical derivation of the optimum triplicator," Opt. Commun. **157**(1-6), 13–16 (1998).
41. A. Niv, G. Biener, V. Kleiner, and E. Hasman, "Rotating vectorial vortices produced by space-variant subwavelength gratings," Opt. Lett. **30**(21), 2933–2935 (2005).
42. A. Niv, G. Biener, V. Kleiner, and E. Hasman, "Manipulation of the Pancharatnam phase in vectorial vortices," Opt. Express **14**(10), 4208–4220 (2006).
43. S. W. Hell and J. Wichmann, "Breaking the diffraction resolution limit by stimulated emission: stimulated-emission-depletion fluorescence microscopy," Opt. Lett. **19**(11), 780–782 (1994).
44. S. W. Hell, "Far-field optical nanoscopy," Science **316**(5828), 1153–1158 (2007).
45. Y. Yirmiyahu, A. Niv, G. Biener, V. Kleiner, and E. Hasman, "Vectorial vortex mode transformation for a hollow waveguide using Pancharatnam-Berry phase optical elements," Opt. Lett. **31**(22), 3252–3254 (2006).
46. Y. Yirmiyahu, A. Niv, G. Biener, V. Kleiner, and E. Hasman, "Excitation of a single hollow waveguide mode using inhomogeneous anisotropic subwavelength structures," Opt. Express **15**(20), 13404–13414 (2007).